Contact Fracture Mechanism of Electroplated Ni-P Coating on Stainless Steel Substrate

Akio Yonezu[1,*], **Michihiro Niwa**[1]

[1] Department of Precision Mechanics, Chuo University, Tokyo 112-8551, Japan
* Corresponding author: akioyonezu.31x@g.chuo-u.ac.jp

Abstract The contact fracture property and mechanism of electroplated Ni-P coating on stainless steel substrate were investigated using ball indentation testing, through a comprehensive experimental and numerical approach. First, the elastoplastic properties of both coating and substrate were evaluated using micro indentation tests. Next, ball indentation test with large contact force was performed, such that the brittle coating on ductile substrate suffers from cracks, including ring crack (propagates circumferentially) and radial cracks (propagates radially), owing to the coating bending effect. The fracture nucleation process was investigated using the acoustic emission technique (AET). In addition, finite element method (FEM) with cohesive zone model (CZM) was carried out to compute stress field and simulate crack initiation around the impression during the test. By using the comprehensive experimental/computational framework, the nucleation process (mechanism) of such a complicate crack system was clarified. The present technique and fracture mechanism may be applicable to the analysis of structural integrity of other brittle coatings.

Keywords Electroplated Ni-P coating, Contact fracture, Ball indentation

1. Introduction

Hard thin films or surface coatings on ductile metallic substrates are often used for contact and slide wear protection. Therefore, the characteristics and mechanism of their contact fracture are critical for ensuring their mechanical performances. Many hard coatings are deposited using the electroplate technique, which may achieve massive production with low cost and large area/ thick deposition (even when the substrate geometry is complicated) [1-5]. Among the electroplated hard coatings, Ni–P material possesses high hardness, high strength and other superior mechanical properties, providing excellent performance (such as wear and corrosion resistance) for metallic ductile substrate/components [2, 6-9]. Thus, characterizing the contact fracture properties of Ni–P coatings is the most important issue regarding structural integrity and application.

Indentation method is convenient way to simulate contact fracture against foreign object. Such a contact loading sometimes shows complicate fracture morphology, such as radial crack, ring crack and lateral crack [13, 14]. These differences are dependent on coating thickness, geometry of indenter, elastoplastic properties of both coating and substrate [15-17], which dictates various types of stress field and the maximum value that are responsible for coating fracture. One of the critical challenges lies in an understanding of the process how several different types of cracks occurs. It may require reliable method to monitor the crack propagation and fracture processes in-situ during indentation test, as well as to effectively analyze the stress field upon indentation loading and during crack propagation.

In this study, ball indentation test was carried out to simulate contact fracture of electroplated Ni-P coating on stainless steel substrate. Acoustic emission technique was utilized to monitor the timing of coating cracks. Stress field upon indentation was computed by finite element method (FEM), where the cohesive element was used to simulate crack nucleation. The comprehensive experimental/numerical approach helps to clarify stress criterion of complicate coating crack system.

2. Materials

In this study, Ni-P alloy was electroplated onto SUS304 in the plating bath. The electrolysis condition is described elsewhere [10]. The coating thickness is about 180 μm. After electroplating, heat treatment of 350°C was performed for one hour in vacuum. According to the reference [9, 10], post-heat treatment is crucial for the mechanical properties of the coating. Initially, the element of P (phosphorus) is a solution in the matrix of Ni, and then NiP_3 (having high hardness) gradually precipitates during post-heat treatment; when the post-heat treatment temperature is between 300 and 350°C, the maximum hardness (*HV*=800 - 1000) is achieved [9, 10] for wear protection, whereas the fracture toughness exhibits the lowest value [9]. Therefore, the investigation of crack morphology and cracking resistance due to contact loading is a critical issue for the Ni-P electroplated coating.

To evaluate mechanical properties (elastoplastic properties) of both Ni-P coating and steel substrate, micro indentation tests against the cross section were performed as shown in Fig. 1(a). Berkovich indenter was used with the maximum force of 100 mN. The representative *F-h* curves were plotted by solid lines in Fig. 1(b). Based on the *F-h* curves, the elastic properties (Young's modulus) were

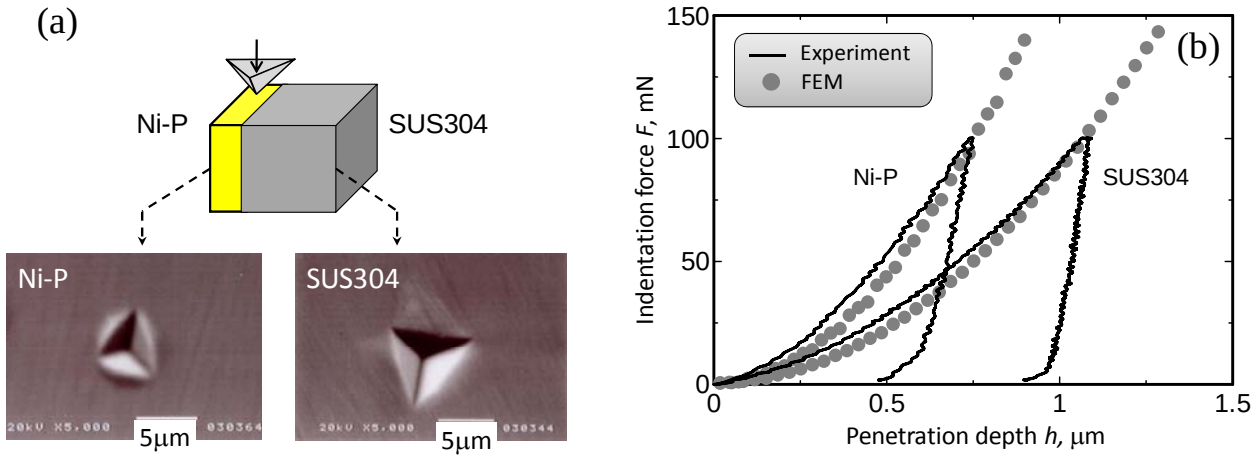

Fig.1 (a) Micro indentation method for cross-section of Ni-P coating and SUS304, and their impressions. (b) Their indentation curves combined with computational ones using finite element method.

Table 1 Mechanical properties of electroplated Ni-P coating and SUS304 substrate.

Material	Young's modulus *E* GPa	Poisson's ratio ν	Hardness H GPa	Yield stress σ_y GPa	Work hardening exponent *n*
Ni-P coating	217	0.37*	7.51	2.40	0.05
SUS304 substrate	175	0.3	3.49	0.22	0.47

* Morikawa et al. The Iron and Steel Institute of Japan (ISIJ), Vol.82, pp.935-940, 1996

estimated by Oliver-Pharr method [18, 19]. Here, the Poisson's ratio of coating is referred to be 0.37 obtained by the surface acoustic wave (SAW) technique [10]. The Young's modulus of coating/substrate shows similar values, i.e. Ni-P coating is 217 GPa, and SUS304 is 175 GPa. Subsequently, the plastic properties (stress - strain relationship) of coating and substrate were estimated by using the reverse analysis ([20, 21]). Here, the plastic properties were assumed with power-law constitutive equation, involving yield stress σ_Y and work hardening exponent n. The estimated results were shown in Table 1. To verify the estimation, finite element simulation (employing these estimated properties) of the micro indentation test was carried out and the resulting indentation curve (F-h) was shown in Fig. 1(b). The simulated results (as indicated by grey circle) agreed well with experimental data for both coating/substrate. This suggested that the estimated elastoplastic properties were robust, and can be employed for stress analysis and crack nucleation subjected deep ball indentation (see Section 5.1). Noted that, according to the reference [9], there might be internal residual stress of Ni-P coating. By using X-ray diffraction, the stress was measured to be almost zero for the present coating (with heat treatment temperature of 350C^o) [9]. Thus, we consider the internal stress-free coating.

3. Experimental Method

Ball indentation tests were performed using an electro-hydraulic testing machine equipped with a ball indenter and two eddy current sensors. The diameter of indenter ball d is 10 mm. The indentation force F gradually increases with the rate of dF/dt = 1 N/s up to the maximum indentation force F_{max} (=1000 N or 2000 N), and sustains the constant value in 50 s, and gradually decreases with the same dF/dt until the force of zero. During the test, acoustic emission (AE) signals were monitored in order to identify the timing of crack nucleation. Four small AE sensors were mounted on the side surfaces of a specimen.

4. Experimental Results

Figures 2 show the micrographs of specimen surface after the test of F_{max}=2000 N. Although the test of F_{max}=1000 N shows no clear crack (however, some friction/ wear tracks were observed), the test of F_{max}=2000 N (Fig. 2) shows complicated coating crack morphology: one type is circumferential crack, namely "ring crack", and the other type initiates from the ring crack and propagate radially, namely "radial crack". There is no delamination (coating spalling) thanks to the strong adhesive strength of the coating/substrate system. The present study therefore focuses on the formation mechanisms of ring crack and radial crack, which may provide useful insights for the mechanical/material design of coating/substrate system.

Figure 3 shows indentation curve of the test with F_{max}=2000 N. The detected AEs were plotted as triangles on the F-h curve in this figure. It is found that the first AE was detected at about F=1200 N and several AEs were subsequently monitored up to about F=1500 N. Furthermore, the unloading process was found to start AE generation from F=1600 N during unloading. Therefore, it is expected that the coating cracks occur during both loading and unloading. Based on these experimental evidences, the stress field is investigated by finite element method in the next section, so as to further clarify the contact cracking behavior.

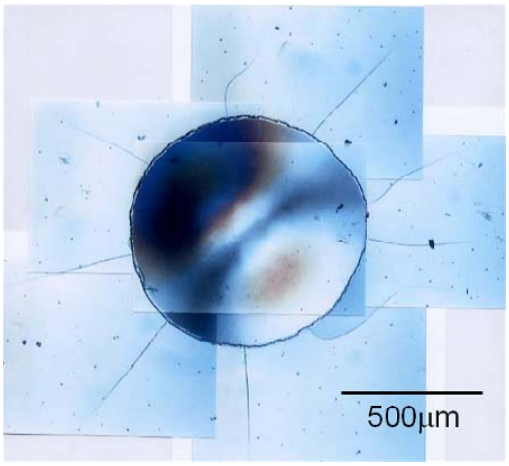

Fig.2 Micrographs of impressions tested with 2000 N.

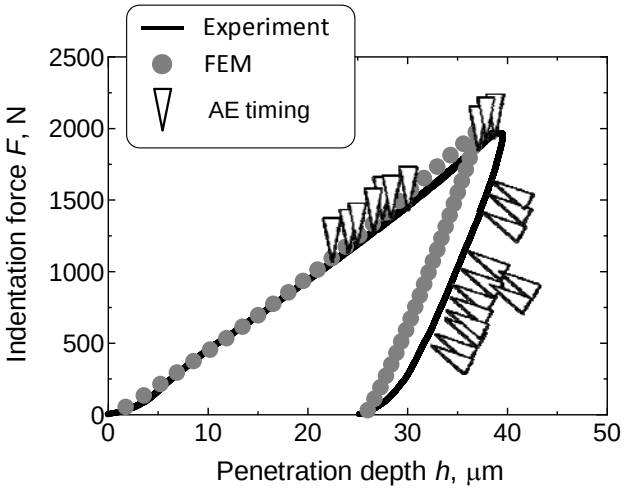

Fig.3 Indentation curve obtained by the test with maximum force of 2000 N. Triangle on the curve indicates the timing of AE generation. In addition, grey circle indicates the simulated indentation curve with finite element method.

5. Discussion

5.1 Crack initiation

By taking advantage of symmetry, an axisymmetric model is established for FEM analysis with the commercial code MARC and MENTAT. The material parameters are taken from Table 1, for both coating and substrate. A rigid ball indenter with radius d=10 mm is employed as a close analog to that used in experiment. To verify both the present FEM model and measured material property, the computed indentation curve is plotted as symbols (grey circle) in Fig. 3, showing reasonable agreement with the experimental curve.

Figure 4 represents a contour map of the indentation stress field computed by FEM simulation when the first AE was detected (as discussed in Fig.3). Fig. 4 (a) shows the map for the radial stress component (σ_{rr}), which is responsible for ring crack, and Fig. 4(b) is the circumferential component ($\sigma_{\theta\theta}$) for radial crack. For σ_{rr}, a large tensile stress (up to about 1.8 GPa) occurs outside the contact region, where the ring crack may be produced if such a tensile stress is sufficiently high. Indeed, such a prominent tensile stress is contributed by the large local bending curvature of the film, assisted by the extensive plastic deformation of the substrate [12, 15, 16]. On the other hand, $\sigma_{\theta\theta}$ (in Fig. 4(b)) is relatively small (less than about 1.0 GPa which is quite lower than the σ_{rr} component). Therefore, the first detected AE should be from ring crack, suggesting that the ring crack initiated first.

The surface distribution of σ_{rr} as a function of the indentation force is given in Fig.5. As expected, the maximum tensile stress increases and shifts outwards with increase in indentation force (deeper penetration), which is associated with the increased coating bending curvature outside the contact zone. When the indentation force reaches the critical value (F = 1200 N), the location of the maximum stress (r = 390 μm) roughly coincides with the radius of the ring crack (as indicated by dashed vertical lines) observed in experiment (see Figs. 2). Thus, we can obtain the critical fracture strength of the coating, σ_C=1.8 GPa. Note that, this value of σ_C is seemed to be the intrinsic strength of the coating (since the present Ni-P coating does not have large internal stress [9], Section 2).

From the above investigations, it is revealed that when a ball indenter makes deep contact with the

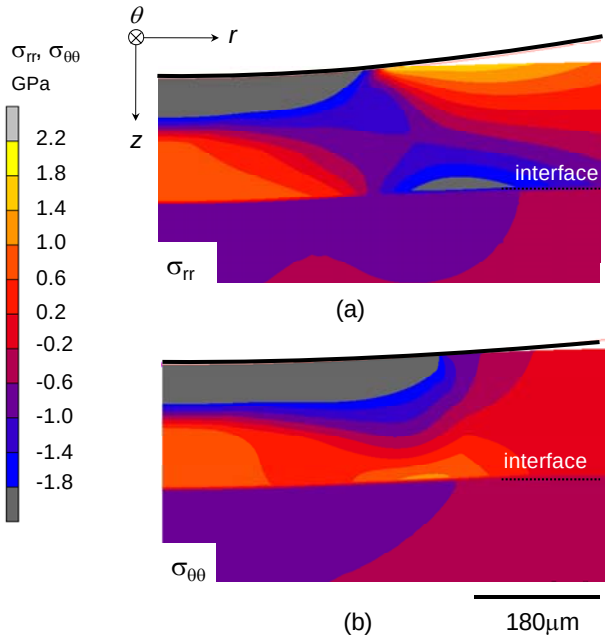

Fig.4 Counter map of stress distribution when the first AE was detected (see Fig.6). (a) normal stress along radial direction, σ_{rr}, and (b) normal stress along circumferential direction, $\sigma_{\theta\theta}$.

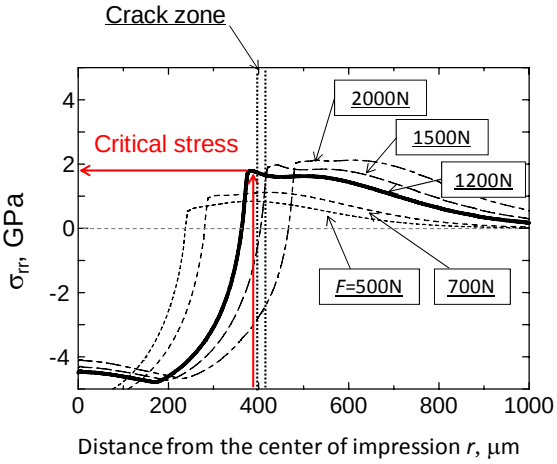

Fig.5 Radial stress σ_{rr} distribution as a function of distance r, with the increases in indentation force. The thick line corresponds to the critical indentation force of 1200 N, when first AE is detected (see Fig.6).

Fig.6 Contour map of CZM damage for ring crack nucleation, when indentation force is about 1200 N.

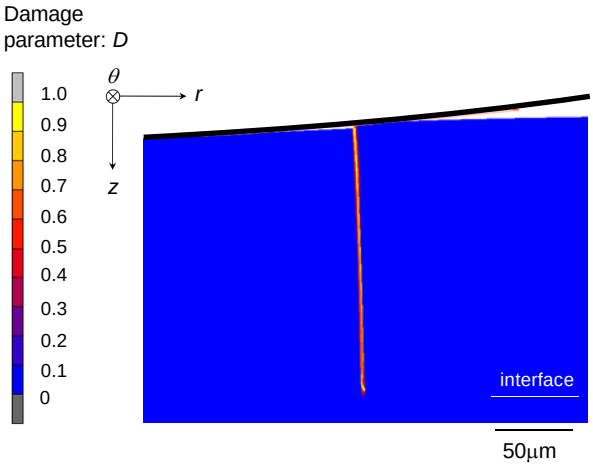

surface of brittle coating, the steel substrate undergoes extensive plastic deformation, which bends the coating and leads to large tensile stress, producing ring crack. Thus, the next question is how the radial crack initiates after the ring crack formation.

5.2 Subsequent crack initiation

To investigate how radial crack forms, the existence of ring crack must be incorporated with stress analysis during indentation. Thus, we employed the cohesive zone model (CZM) in the FEM to compute the stress field in conjunction with ring crack formation.

The CZM is applicable to both ductile and brittle materials [23-29]. The CZM essentially models the fracture process zone in a plane ahead of the crack tip. The zone is assumed to be subjected to cohesive traction. The model usually describes the gradual degradation of the adhesion between two regions along the crack propagation plane. The mechanical response of the cohesive zone obeys a

traction–separation law that yields the relationship between the separation distance v of the two material faces at an interface and the traction stress σ acting between them. Although numerous traction–separation laws for the cohesive zone element have been proposed, this study employed an exponential law (called the Smith-Ferrante type [24]) due to its simplicity. This exponential law requires two independent materials parameters, i.e. the maximum stress σ_{max} and the crack growth resistance K_C. Since the σ_{max} roughly corresponds to the critical stress (fracture strength), σ_{max} is set to be 1.8 GPa from Fig. 5. However, the other parameter K_C is unknown. Thus, several values (0.5, 1.0 and 5.5 MPa $m^{1/2}$) were employed to simulate ring crack formation.
To compute the stress field involving ring crack formation, we introduced CZM element into FEM model. Here, the CZM elements are implemented at the location where the ring crack forms (r=400 μm in Fig.2 and Fig.5). Figure 6 shows the contour map of damage parameter D around the impression (when D becomes one, crack completely forms [22, 24]). When K_c=5.5 MPa $m^{1/2}$, as shown in Fig.6, the ring crack (due to σ_{rr} component) propagates from the surface to the interface. In fact, actual crack was found to propagate up to the interface from the cross sectional observation. (Note that the choice of Kc value does not affect the subsequent stress field after crack propagation.)

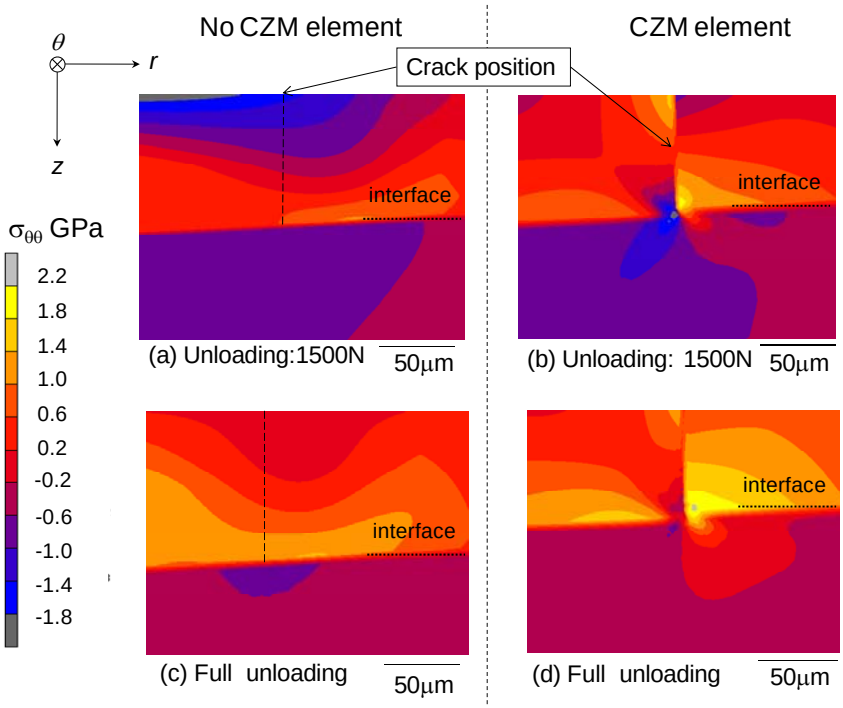

Fig.7 Contour map of stress $\sigma_{\theta\theta}$ distribution around the impression during indentation loading: homogenous model with no CZM element ((a),(c)) and model with CZM element ((b),(d)). (a) and (b) shows the map at F= 1500 N (F/F_{max}=0.75), while (c) and (d) is at the maximum force (F_{max}=2000 N). 1200 N.

5.3 Mechanism of cracking system

Figure 7 shows the snapshot of the normal stress $\sigma_{\theta\theta}$ distribution during the loading process. Fig. 7 (a) and (b) show the stress field at F=1500 N, whereas Fig. 7 (c) and (d) show the result at the maximum indentation force (2000 N). For comparison, the model with no cohesive zone element was also computed, as shown in Fig. 7(a) and (c). This model simulates the stress field due to

indenter contact, and does not induce any crack formation. Thus, $\sigma_{\theta\theta}$ (in Figs.7(a)(c)) does not show large tensile stress, which is the same trend with Fig.4(b). On the other hand, the model with CZM element in Figs.7(b)(d) exhibits different $\sigma_{\theta\theta}$ stress field, owing to the ring crack formation. In particular, possible area for large tensile $\sigma_{\theta\theta}$ develops near the interface.

Figures 8 shows a snapshot of $\sigma_{\theta\theta}$ distribution during unloading process, in a similar fashion with Fig.7. In Figs.8 (a) and (c), without the CZM element model there is no large $\sigma_{\theta\theta}$ distribution, whereas with the CZM element, the significant larger $\sigma_{\theta\theta}$ develops at the right side of crack path near interface, and its magnitude increases during the unloading process and reaches the maximum value upon full unloading. Therefore, it is found that ring crack formation significantly changes the subsequent stress field during the indentation, in particular the large $\sigma_{\theta\theta}$ upon unloading, and the radial crack is seemed to initiate at the right side of crack path.

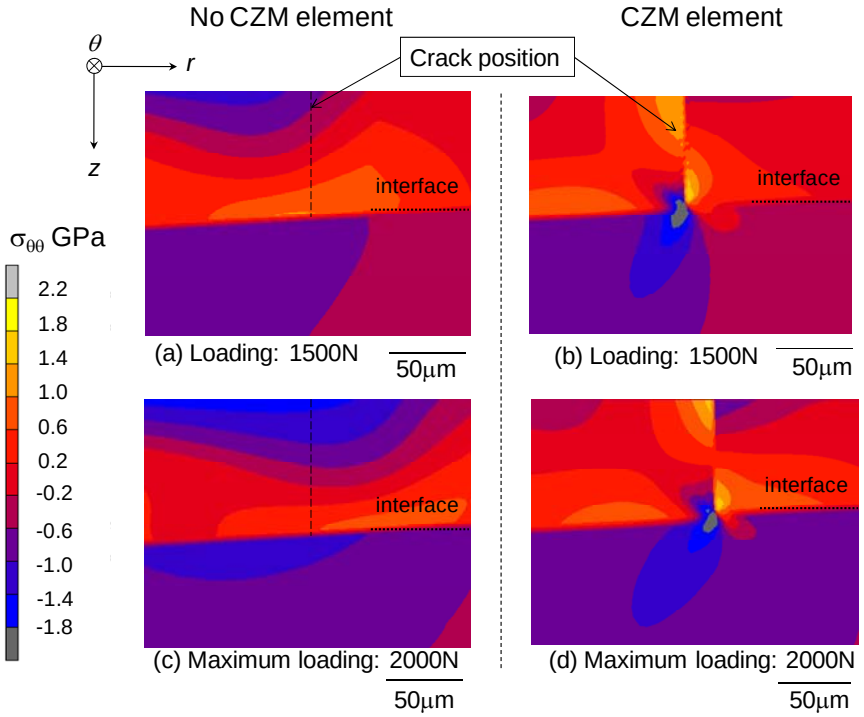

Fig.8 Contour map of stress $\sigma_{\theta\theta}$ distribution around the impression during indentation unloading: homogenous model with no CZM element ((a),(c)) and model with CZM element ((b),(d)). (a) and (b) shows the map at F=1500 N (F/F_{max}=0.75), while (c) and (d) is at the full unloading (F=0 N).

Figure 9 shows the stress $\sigma_{\theta\theta}$ distribution along the crack path with respect to the distance from coating surface to interface. The four curves indicate the results of 1500 N and 2000 N (loading) and 1500 N and 0 N (unloading). While the overall $\sigma_{\theta\theta}$ magnitude increases during the unloading process, the position of the maximum $\sigma_{\theta\theta}$ does not change (at about 175 μm below the surface). Finally, the change in the maximum $\sigma_{\theta\theta}$ value is investigated as a function of the indentation force (during unloading process) in Fig.10. As expected, the maximum $\sigma_{\theta\theta}$ increases with decreasing indentation force. Referring to Fig.3, the AE occurrence was seen at about F=1600 N under unloading. In Fig.10, this force (F=1600 N) corresponds to $\sigma_{\theta\theta}$ = 1.82 GPa, which is reasonably agreement with the critical stress σ_{rr} for ring crack in Fig.5. Therefore, it is found that radial crack is produced by $\sigma_{\theta\theta}$, which develops near the interface and ring crack path, suggesting that ring crack formation (during loading) is crucial for subsequent radial crack nucleation during unloading.

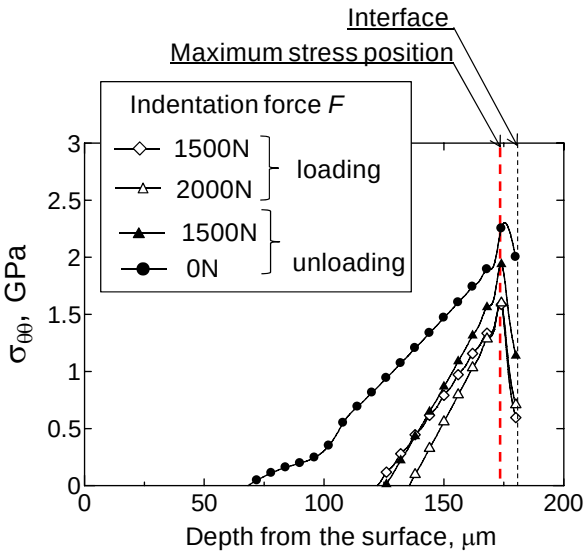

Fig.9 Stress $\sigma_{\theta\theta}$ distribution along the ring crack path (the depth from coating surface to interface). Four lines with various symbols indicate the results of 1500 N and 2000 N (loading process) and 1500 N and 0 N (unloading process).

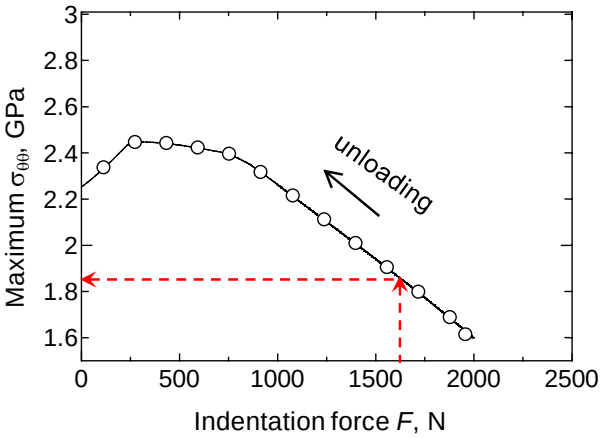

Fig.10 Changes in maximum stress $\sigma_{\theta\theta}$ (in Fig.9) as a function of indentation force during unloading.

6. Conclusion

This study investigated the contact fracture property of electroplated Ni-P coating on stainless steel substrate, which is important for its application as contact/sliding member for wear resistance. Ball indentation test with large contact/indentation force produces two types of cracks in the coating, namely the ring crack and radial crack. To elucidate the fracture process, acoustic emission technique (AET) was employed to identify the timing of crack initiation during the test. In addition, finite element method (FEM) was carried out to compute the stress field around the impression during the test. The cohesive zone modeling (CZM) was embedded with FEM to simulate the crack interaction. It is found that the ring crack first initiates during loading process, due to tensile radial stress (owing to the coating bending effect). Subsequently, radial crack nucleates from ring crack path (i.e. near ring crack tip at interface) due to the large circumferential stress developed upon unloading.

By using the comprehensive experimental/computational indentation framework (combined with AE and FEM), the mechanism of the complicate coating crack system is clarified, and the stress criterion for each cracking system is quantified. Based on these findings, further systematic study may suggest how to control or prevent the coating cracks. This will become useful guidance for material design in coating industry. The comprehensive experimental/computational framework is also applicable to other coating/substrate systems.

Acknowledgements

The work of A.Y. is supported in part of Grant-in-Aid for Young Scientist of (B) (No. 22760077) of

the Ministry of Education, Culture, Sports, Science and Technology, Japan, and Research Grant for Science and Technology of SUZUKI Foundation

References

[1] K.-H. Hou, M.-C. Jeng, M.-D. Ger, Wear 262 (2007) 833-844.
[2] H. Tian, N. Saka, E. Rabinowicz, Wear 142 (1991) 51-85.
[3] Z. Ping, J. Yuan, Y. He, X. Li, Acta Metall. Sin. (Engl. Lett.) 22 (2009) 225-232.
[4] Y. D. He, H. F. Fu, X. G. Li, W. Gao, Scri. Mater. 58 (2008) 504-507.
[5] P. Peeters, G. Hoorn, T. Daenen, A. Kurowski, G. Staikov, Electrochim. Acta 47 (2001) 161-169.
[6] S.-H. Kim, Mater. Lett. 61 (2007) 3589-3592.
[7] W. Sha, J.-S. Pan, J. Alloys Compds. 182 (1992) L1-L3.
[8] W. Sha, P. J.-S., J. Less-Common Metals 166 (1990) L11-L13.
[9] T. Yashiki, T. Nakayama, J. Kato, The Iron and Steel Institute of Japan 81 (1995) 48-53.
[10] Y. Morikawa, H. Cho, T. Nakayama, M. Takemoto, The Iron and Steel Institute of Japan 82 (1996).
[11] A. Yonezu, B. Xu, X. Chen, Mater. Sci. Eng. 507 (2009) 226-235.
[12] A. Yonezu, B. Xu, X. Chen, Thin Solid Films, 518 (2010) 2082–2089.
[13] R. F. Cook, G. M. Pharr, J. Am. Ceram. Soc. 73 (1990) 787-817.
[14] X. Chen, J. W. Hutchinson, A. G. Evans, J. Am. Cer. Soc. 88 (2005) 1233-1238.
[15] B. R. Lawn, Y. Deng, P. Miranda, P. Pajares, H. Chai, D. K. Kim, J. Mater. Res. 17 (2002) 3019-3035.
[16] H. Chai, B. R. Lawn, J. Mater. Res. 19 (2004) 1752-1761.
[17] A. Yonezu, H. Cho, T. Ogawa, M. Takemoto, Sci. Tech. Adv. Mater. 7 (2006) 97-103.
[18] W. C. Oliver, G. M. Pharr, J. Mater. Res. 7 (1992) 1564-1583.
[19] W. C. Oliver, G. M. Pharr, J. Mater. Res. 19 (2004) 3-20.
[20] N. Ogasawara, N. Chiba, X. Chen, Scripta Materialia 54 (2006) 65-70.
[21] A. Yonezu, X. Chen, Dia. Relat. Mater.19 (2010) 40-49.
[22] Marc, Marc 2010, Theory and User's Manual A 2010.
[23] N. Chandra, H. Li, C. Shet, H. Ghonem, Int J Solids Struct 39 (2002) 2827-2855.
[24] B. A. E. Hal, R. H. J. Peerlings, M. G. D. Geers, O. Sluis, Microelectronics Reliability 47 (2007) 1251-1261.
[25] Z. Xia, W. A. Curtin, B. W. Sheldon, Acta Mater. 52 (2004) 3507-3517.
[26] V. Tvergaard, J. W. Hutchinson, J. Mech. Phys. Solids 40 (1992) 1377-1397.
[27] G. I. Barenblatt, Advances in Applied Mechanics 7 (1962) 56-129.
[28] V. Olden, C. Thaulow, R. Johnsen, E. Østby, T. Berstad, Eng. Fract. Mech. 75 (2008) 2333-2351.
[29] A. Yonezu, T. Hara, T. Kondo, H. Hirakata, K. Minoshima, Mater. Sci. Eng. A 531 (2012) 147–154